





Submillimeter Radiation as the Thermal Component of the Neupert Effect

Jorge F. Valle Silva¹  ·
C. Guillermo Giménez de Castro^{1,2}  ·
Paulo J. A. Simões^{1,3}  ·
Jean-Pierre Raulin¹ 

© Springer

Abstract The Neupert effect is the empirical observation that the temporal evolution of non-thermal emission (*e.g.* hard X-rays) is frequently proportional to the time derivative of the thermal emission flux (soft X-rays), or vice versa, that time-integrated non-thermal flux is proportional to thermal flux. We analyzed the GOES M2.2 event SOL2011-02-14T17:25, and we found that the 212 GHz emission plays quite well the role of the thermal component of the Neupert effect. We show that the maximum of the hard X-ray flux for energies above 50 keV is coincident in time with the time-derivative of the 212 GHz flux, within the uncertainties. The microwave flux density at 15.4 GHz, produced by optically thin gyrosynchrotron mechanism, and hard-X rays above 25 keV mark the typical impulsive phase, and they have similar time evolution. On the other hand, the 212 GHz emission is delayed by about 25 seconds with respect to the microwave and hard X-ray peak. We argue that this delay cannot be explained by magnetic trapping of non-thermal electrons. With all of the observational evidence, we suggest that the 212 GHz emission is produced by thermal bremsstrahlung, initially in the chromosphere, and shifting to optically thin emission from the hot coronal loops at the end of the gradual phase.

Keywords: Flares, Dynamics; Flares, X-Rays; Flares submillimeter radiation; chromospheric evaporation

✉ C.G. Giménez de Castro
guigue@craam.mackenzie.br

¹ Centro de Rádio Astronomia e Astrofísica Mackenzie, Escola de Engenharia, Universidade Presbiteriana Mackenzie, Rua da Consolação 896, 01302-907, São Paulo, Brazil

² Instituto e Astronomía y Física del Espacio, CONICET-UBA, CC. 67 Suc. 28, 1428, Buenos Aires, Argentina

³ SUPA School of Physics & Astronomy, University of Glasgow, Glasgow, G12 8QQ, Scotland

1. Introduction

The different temporal evolution of hard X-rays (HXR) and soft X-rays (SXR) during impulsive bursts is known since the *Orbiting Solar Observatory*-1 (OSO-1) observations (White, 1964). Moreover, OSO-1 data also showed that microwaves (MW) and HXR are time coincident during the impulsive bursts (Frost, 1964), lending support to their close origin. It was Neupert (1968) who noted for the first time that the SXR flux is better correlated with the time-integrated flux density (fluence) at the MW frequency $\nu = 2.695$ GHz, *i.e.*

$$F_{\text{SXR}}(t) \propto \int_{t_0}^t F_{\text{MW}}(t') dt' , \quad (1)$$

where F_{SXR} is the SXR flux and F_{MW} is the MW flux density. This relation holds until F_{SXR} reaches its maximum flux, which should be coincident with the end of the MW emission. A similar relation is observed between HXR and SXR (Hudson, 1991). This observational fact was interpreted as the atmospheric response to the heating produced by the energetic particles when they precipitate into the lower and denser layers: energetic electrons spiraling within the magnetic fields produce synchrotron radiation observed at MW, while the HXR is non-thermal bremsstrahlung produced by Coulomb collisions, transferring energy to the plasma that expands and emits thermal bremsstrahlung observed at SXR: a phenomenon also known as chromospheric evaporation (Neupert, 1968; Hudson and Ohki, 1972; Antonucci, Gabriel, and Dennis, 1984). Conversely, Equation 1 can be written in terms of the SXR time derivative (Hudson, 1991):

$$\frac{dF_{\text{SXR}}(t)}{dt} \propto F_{\text{MW}}(t) , \quad \text{or} \quad \frac{dF_{\text{SXR}}(t)}{dt} \propto F_{\text{HXR}}(t) . \quad (2)$$

Equations 1 and 2 are the mathematical representation of the Neupert effect. Statistical analysis of SXR and HXR data show that in around half of the bursts the effect is present, which means that for around 50 % of the cases, there is evidence for a more complex heating mechanism than only electron-beam-driven (Veronig *et al.*, 2002a). Furthermore, McAteer and Bloomfield (2013) analyzed the energy band pairs for which the Neupert effect is better observed, concluding that the best agreement is between the bands 12–25 keV (SXR) and 100–300 keV (HXR).

All of the works mentioned concentrate on the SXR wavelength domain to observe the thermal emission. Trotter *et al.* (2000) observed that H α has a slow (accumulative) and fast (direct) relationship with HXR: either chromospheric evaporation or continuous coronal heat flux may be responsible for the slow response. In another statistical work, Veronig *et al.* (2002b) analyzed the timing between SXR, HXR, and H α , showing that in 90 % of all cases, SXR starts before HXR while H α starts simultaneously with HXR. Moreover, SXR and H α maximum fluxes are temporally coincident with the end of HXR.

Solar flare observations at submillimeter frequencies (here considered to be frequencies > 100 GHz) are relatively new. For this reason the physical origin of the emission is still a subject of debate. Thermal bremsstrahlung and synchrotron

radiation, or a combination of both, are the main candidate sources of radiation at high frequencies (see, *e.g.*, Bastian, Benz, and Gary, 1998; Pick and Vilmer, 2008). Other mechanisms have been suggested (Kaufmann and Raulin, 2006; Fleishman and Kontar, 2010; Krucker *et al.*, 2013), but the lack of a better spectral coverage toward the THz range does not allow us to draw definitive conclusions. In the work of Trottet *et al.* (2002, 2011), Lüthi, Magun, and Miller (2004), and Lüthi, Lüdi, and Magun (2004) the submillimeter radiation during the time-extended or gradual phase of the solar flares was compatible with thermal bremsstrahlung, while during the impulsive phase it was considered of synchrotron origin. Moreover Tsap *et al.* (2016) have shown a particular flare whose emission between 93 and 140 GHz increases and can be attributed solely to thermal bremsstrahlung.

We present in this work a peculiar event where submillimeter emission can be interpreted as the thermal component of the Neupert effect. We show that the 212 GHz time profile is very different from the time profiles at HXR and MW, that it does not show the typical impulsive phase (Krucker *et al.*, 2013), and that its temporal evolution is in agreement with both Equations 1 and 2. In contrast to other events (Lüthi, Magun, and Miller, 2004; Lüthi, Lüdi, and Magun, 2004; Trottet *et al.*, 2011, 2015) the submillimeter time-extended temporal evolution is not well correlated with SXR.

2. Observations and Data Analysis

The event SOL2011-02-14T17:25 (hereafter SOL2011-02-14 for simplicity) is associated with a GOES M2.2-class SXR flare in the Active Region 11158. On 14 February, at 0 UT, the region was located at Heliographic Latitude S20 and Longitude W04, it was 10° wide in longitude, and within it occurred several C-class events before the M2.2, subject of the present analysis. The Solar Submillimeter Telescope (SST: Kaufmann *et al.*, 2008) tracked AR11158 since the day before the event. On 14 February, the atmospheric conditions were not favorable for millimeter observations: at 212 GHz the zenith optical depth was 0.8, and we can only estimate the lower limit for the optical depth at 405 GHz to be ≈ 4.5 . Therefore, at the antenna elevations during the event, the signal was attenuated 57% and $> 99\%$ at 212 and 405 GHz respectively. In addition to this correction, the antenna temperatures of the multi-beam array (Beams 2,3 and 4) were subtracted by the antenna temperature of Beam 1, which is $7'$ far from the array (see Trottet *et al.*, 2011, for a detailed explanation). While in this way we remove most of the atmospheric fluctuations, we note that since Beam 1 is off the active region, a variation in opacity is less amplified by the *cool* background than the same variation observed by Beams 2, 3 and 4 which are over the *hot* active region. However, at 212 GHz active regions are at most 20% hotter than quiet Sun (Silva *et al.*, 2005), and therefore this is a limited effect within the quoted uncertainty.

The SST observed the flare at 212 GHz with the three beams that compose its multi-beam system providing the instantaneous emitting centroid and its flux density every 0.04 seconds using the technique described in Section 2.3. The flux

density reaches its maximum between 17:25:45 and 17:25:52 UT (see Figure 1), with mean $\langle Fx_{212} \rangle_{\max} = 220 \pm 30$ SFU. The peak is relatively smooth, temporal fluctuations around the maximum have a standard deviation of about 4% of $\langle Fx_{212} \rangle_{\max}$.

After the peak, the flux density decreases slowly; the event overall duration is \approx nine minutes. At 405 GHz no significant signal excess was detected, a logical consequence of the high optical depth. A rough estimation of the detectable source flux threshold was obtained from the measured antenna temperature fluctuations, $\delta T_{405} \approx 15$ K, corrected by optical depth and for the beam offset (that we can infer from the multi-beam solution) and converted to flux. The result yields $Fx_{405} \gtrsim 10^4$ SFU. This number should be considered our uncertainty in the 405 GHz flux.

The flare has been detected in HXR by the *Gamma-Ray Burst Monitor* (GBM) onboard *Fermi* (Meegan *et al.*, 2009). GBM is composed of twelve sodium-iodide (NaI) and two bismuth-germanium-oxide (BGO) detectors. In our analysis we used the NaI 128 energy channels in the range from 4 keV to 2000 keV and 1.024 second time resolution. Unfortunately there are no *Ramaty High Energy Solar Spectroscopic Imager* (RHESSI) data during the impulsive phase of the event. We complement our analysis with MW from the United States Air Force (USAF) *Radio Solar Telescope Network* (RSTN: Guidice *et al.*, 1981) at 1.415, 2.695, 4.995, 8.8, and 15.4 GHz with one-second temporal resolution, and GOES 1–8 Å (1.5–12 keV) with two-second temporal resolution.

2.1. Temporal Evolution

Figure 1 presents a selection of the different frequency / energy temporal profiles. By using GOES and *Fermi* low energy channels, we cover the whole SXR domain. At the lowest energies, GOES 1.5–12 keV the emission has a smooth evolution starting at 17:23 UT, with a simple structure peaking at 17:26 UT, and returning to pre-flare level not before 18:40 UT. *Fermi* 12–25 keV band starts and ends with GOES 1–8 Å, but it shows two peaks: at 17:25:20 UT and at around 17:26:40 UT. On the other hand the impulsive phase at MW and HXR, have a common shape, with delays of less than one second between the strongest structures. Emission starts at around 17:24 UT and ends by 17:27 UT.

A closer look at the temporal evolution at different frequencies and energy bands can be seen in Figure 2, where the fluxes are normalized to facilitate the comparison. In the left panel we present the normalized flux at 212 GHz (shaded dark gray), 15.4 GHz (shaded light gray) and 100–300 keV HXR (black curve). We observe that during the impulsive phase, defined by HXR, there is an excellent match between features observed at HXR and 15.4 GHz, with no detectable delay. This implies that 15.4 GHz has an optical depth $\tau \lesssim 1$, *i.e.* is near the peak of the spectrum. In contrast, the submillimeter emission is, as noted before, smoother, almost featureless, and its peak is delayed by > 20 seconds with respect to HXR. The cross correlation between HXR and 15.4 GHz (HXR and 212 GHz), graphically exposed in the inset with a continuous line (dashed line) are a quantitative way to remark the coincidence (lack of coincidence) of the temporal evolution at different frequencies. The cross correlation between

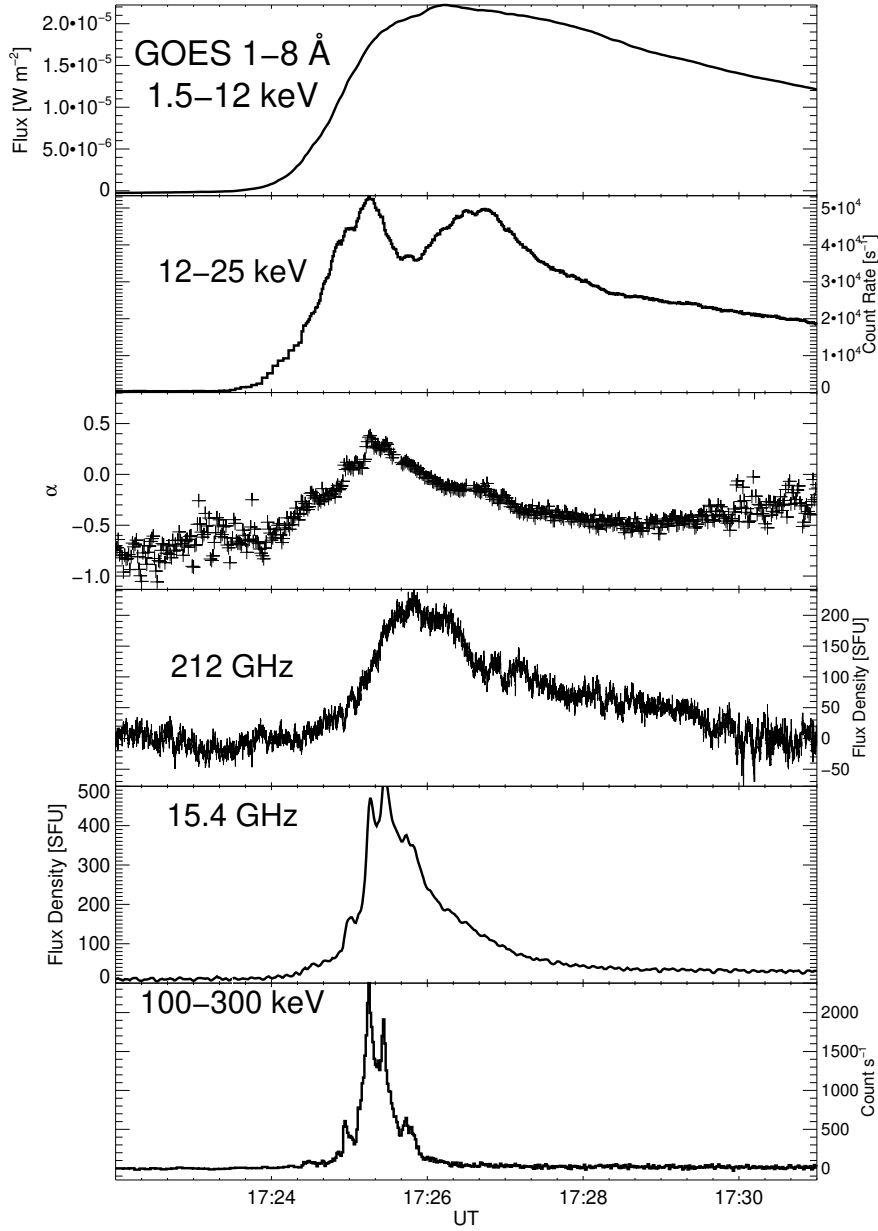


Figure 1. Temporal evolution at selected frequencies / energies. From *top to bottom*: GOES 1–8 Å (1.5–12 keV); *Fermi* GBM NaI 12–25 keV, spectral index α obtained between 15.4 and 212 GHz (see Sec. 2.2), SST 212 GHz, RSTN 15.4 GHz, and *Fermi* GBM NaI 100–300 keV HXR.

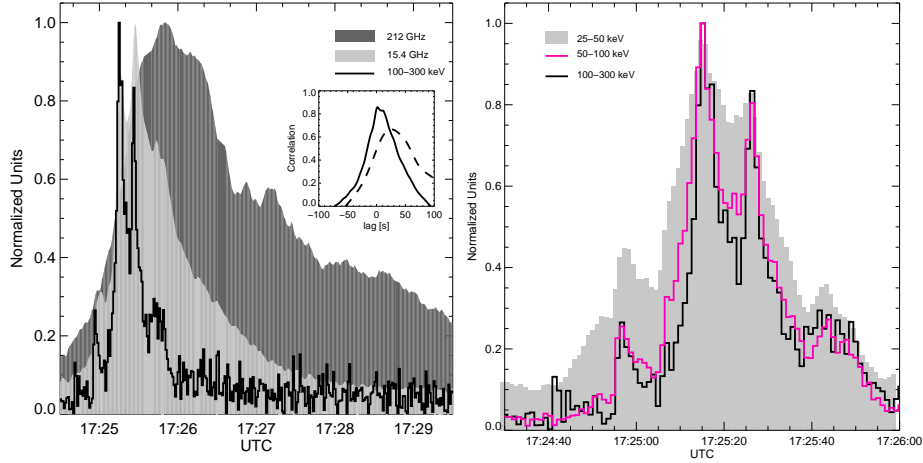


Figure 2. *Left:* Normalized intensities at 212 GHz (shaded dark gray), 15.4 GHz (shaded light gray) and 100–300 keV (black curve). In the inset, the cross correlation as a function of the lag between 100–300 keV and 15.4 GHz (continuous curve) and between 100–300 keV and 212 GHz (dashed curve). *Right:* Normalized count rates at 25–50 keV (shaded light gray), 50–100 keV (magenta curve) and 100–300 keV (black curve).

HXR and 15.4 GHz is maximum for a lag=0 seconds, while between HXR and 212 GHz is maximum for a lag=25 seconds. We have also compared the temporal evolution at the three HXR energy bands (right panel in Figure 2). The shaded light-gray curve represents the lowest energy (25–50 keV), the dark-gray curve the middle energy (50–100 keV) and the black curve the highest detected energy (100–300 keV). All of the peaks match well; therefore we do not observe any delay within the data temporal resolution.

2.2. Spectra

The *Fermi* GBM HXR fitted photon spectrum during the peak time four-second interval (17:25:24 – 17:25:28 UT) is shown in Figure 3 (left panel). The spectrum is best fitted by a thermal component (dot-dashed curve) with temperature $T = 13$ MK and emission measure $EM = 56 \times 10^{49} \text{ cm}^{-3}$, plus a thick-target component from a power-law distribution of electrons, with an electron rate of $F = 2.6 \times 10^{35} \text{ s}^{-1}$, spectral index $\delta = 4.6$; and low-energy cutoff $E_c = 16$ keV (continuous gray curve). From the figure it can be seen that for energies > 20 keV the emission can be considered as non-thermal bremsstrahlung, and that there is no detected emission above ≈ 200 keV.

The radio spectra at different temporal intervals of one-second duration are shown in Figure 3 (right panel). No firm conclusion can be drawn about the submillimeter emission origin during the maximum of the microwave emission, intervals b to d, because of the gap between 15.4 and 212 GHz. For the same reason we cannot determine the peak frequency, but, as noted before, the emission at 15.4 GHz has an optical depth $\tau_{15.4} \lesssim 1$. After the maximum, intervals e and f, flux density at 8.8, 15.4 and 212 GHz are very similar, which can be considered an indication of pure thermal emission. Moreover, while the 15.4 GHz flux

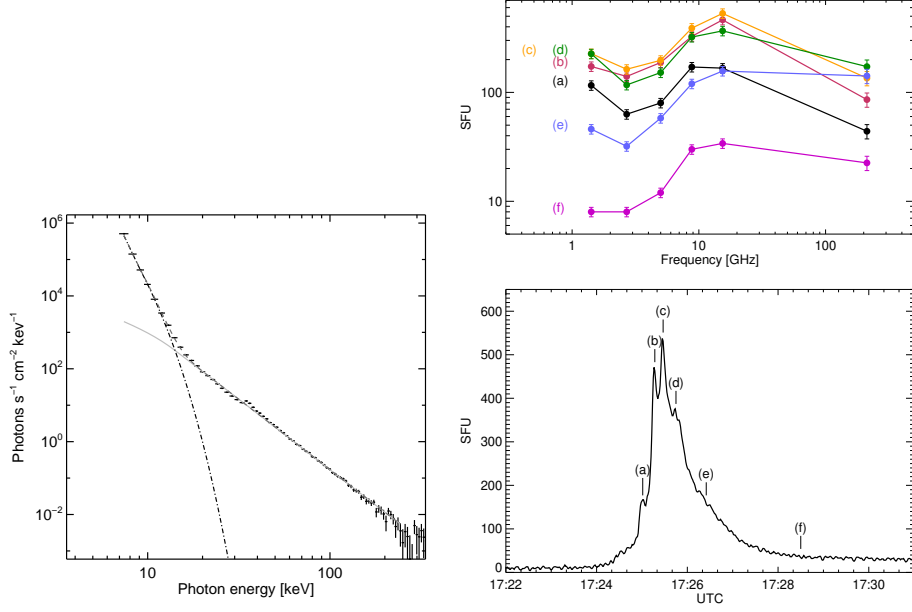


Figure 3. *Left:* HXR photon spectrum at peak time (17:25:24 – 17:25:28 UT), the *dashed gray curve* is the fitted photon spectrum, *continuous thick gray* represents the single power law component, and the *dot-dashed* curve is the thermal radiation. *Top right:* Radio spectra at selected one-second intervals during the impulsive phase of the flare. *Bottom right:* 15.4 GHz time profile with the selected spectral intervals (a to f) identified.

varies by a factor of around 15 between interval c through f, the submillimeter emission just halves its flux during the same period. As an illustration of this behavior we show in Figure 1 the spectral index between 212 and 15.4 GHz $\alpha = -\log(F_{212}/F_{15.4})/\log(212/15.4)$ as a function of time. We remark the fact that $|\alpha| \leq 0.5$ which is a rather hard index. Indeed, applying the Dulk (1985) semi-empirical formulation for gyrosynchrotron emission, we get an electron index $\delta \leq 1.9$. Moreover, we note that during interval a, before the peak, $\alpha < 0.5$ (and $\delta < 2$), indicating again the thermal origin of the 212 GHz emission.

2.3. Submillimeter Position

In order to obtain position and flux for our submillimeter observations we used the iterative multi-beam technique first introduced by Herrmann *et al.* (1992) for observations made with the 13.7-m antenna of the *Itapetinga Radio Observatory* and later applied to SST observations by Cristiani *et al.* (2007). The original method considered point-like sources, and therefore it needed at least three independent observations. Lüthi, Lüdi, and Magun (2004) expanded this method by introducing extended sources, for which they obtained position, flux, and an effective area using four independent observations in order to get a unique solution. In our case we used a matrix representation of the beams obtained after the deconvolution of solar maps observed in 2006 following the method developed by Costa *et al.* (2002). We also considered Gaussian extended sources

defined by a four-tuple (F_s, x, y, σ_s) with F_s the maximum of the source flux density, x, y its position, and σ_s its Gaussian standard deviation.

The iterative method compares a combination of measured and model-calculated relative fluxes of the three different receivers:

$$Q(t_i, x, y, \sigma_s) = \sum_k \left| \frac{F_k^{\text{meas}}(t_i)}{F_{p \neq k}^{\text{meas}}(t_i)} - \frac{F_k^{\text{cal}}(t_i, x, y, \sigma_s)}{F_{p \neq k}^{\text{cal}}(t_i, x, y, \sigma_s)} \right|, \quad (3)$$

$$F_k^{\text{meas}}(t_i) = 2 \frac{k_B T_k(t_i)}{A_e},$$

with $T_k(t_i)$ the antenna excess temperature of beam k at instant t_i ; k_B , A_e the Boltzmann constant and the antenna effective area respectively and $F_k^{\text{cal}}(t_i, x, y, \sigma_s)$ the corresponding calculated flux obtained after convolving the source with the beam. We then looked for the location (x_o, y_o) that overall minimizes Q matrices along the whole event for a fixed source size. Namely

$$\mathcal{Q}(x, y, \sigma_s) = \sum_i Q(t_i, x, y, \sigma_s), \quad \left. \frac{\partial^2 \mathcal{Q}(x, y, \sigma_s)}{\partial x \partial y} \right|_{\sigma_s} = 0. \quad (4)$$

We prepared low-resolution profiles taking values every 15 seconds between 17:24:00 UT and 17:30:00 UT, as is shown in Figure 4. A grid of $350'' \times 350''$ with $10''$ spacing between points is used to calculate $Q(t_i, x, y, \sigma_s)$. The resulting $\mathcal{Q}(x_o, y_o, \sigma_s)$ values, normalized to 100, as a function of the source angular radius $\varphi = \sigma_s \sqrt{\ln(4)}$ are shown in Figure 4 (circles). We note that \mathcal{Q} decreases when the source increases in size up to $25''$, then stabilizes, *i.e.* the method becomes insensitive to changes in size. The same figure also shows the distance from (x_o, y_o) to the center of the biggest and brightest UV source (diamonds). We observe a similar behavior, when the source achieves a size of $\approx 30''$, the distance stabilizes around $10''$. We conclude that that $\varphi \geq 25''$, which corresponds to a source area $A_{\text{MB}} \geq 3.8 \times 10^{17} \text{ cm}^2$. We remark that, since we do not have four independent observations, we cannot provide a unique solution such those obtained by Lüthi, Lüdi, and Magun (2004), or even by Giménez de Castro *et al.* (1999) who worked with analytical expressions and nominal beams.

In Figure 5 the submillimeter centroid position for 17:24:00 and 17:30:00 UT period is shown over a 1700 \AA UV image as a red cross; the dashed red circle represents its absolute uncertainty. The small green cross labeled UV marks the centroid position of the brightest and biggest UV source, and it is the reference for the distance to the submillimeter solutions. The excess flux of the source was obtained after its position and size were determined.

3. Origin of the submillimeter emission

The most common hypothesis for the millimeter and submillimeter emission during the impulsive phase of solar flares is gyrosynchrotron from non-thermal electrons. The same electrons should produce HXR, implying similar HXR and

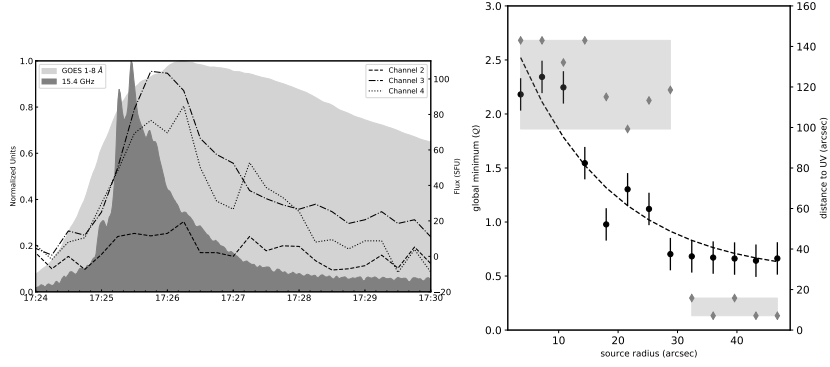


Figure 4. *Left:* Calibrated low-resolution flux density temporal profiles used to determine the source flare position. The dataset was built picking values every 15 seconds between 17:24:00 and 17:30:00 UT for every receiver of the 212 GHz multi-beam array. Normalized light curves from GOES 1–8 Å and RSTN 15.4 GHz are shown for comparison. *Right:* $Q(x_o, o, \sigma_s)$ normalized to 100 as a function of $\varphi = \sigma_s \sqrt{\ln(4)}$ (filled circles), the dashed curve shows the global trend. The diamonds represent the distance between the source positions determined with the multi-beam technique (x_o, y_o) as a function of φ .

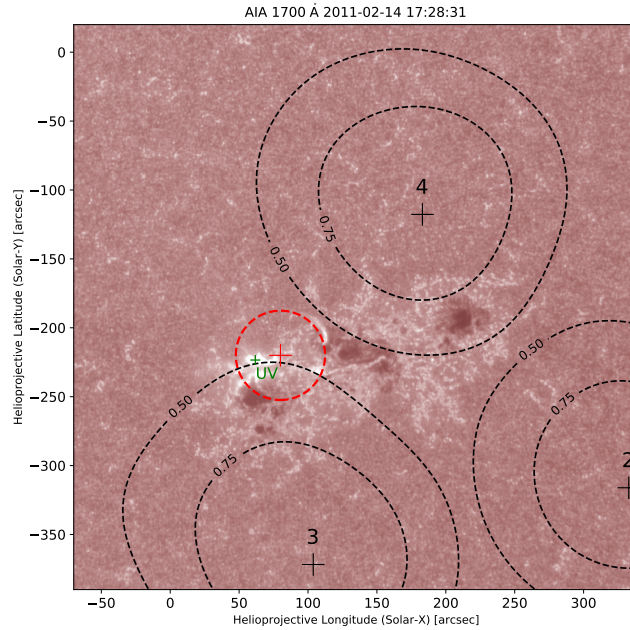


Figure 5. UV image at 1700 Å taken by SDO/AIA at 17:28:31 UT, to avoid the saturated pixels. The red cross is the solution of the iterative multi-beam technique, the dashed red circle is its absolute uncertainty. The small green cross shows the center of the brightest and biggest UV source. The dashed black curves are the three 212 GHz beams used in the multi-beam solution represented at 50% and 75% levels; black crosses are the beam centers.

radio light curves; when delays between them appear, some trapping is considered responsible. However, in this particular case we do not find evidence of gyrosynchrotron and trapping in the lightcurves. Our arguments supporting this conclusion are:

- i)* the temporal evolution at 15.4 GHz greatly differs from that at 212 GHz, that can be hardly attributed to a ≈ 25 s electron trapping in the magnetic loop. Had the emission at both frequencies been produced by gyrosynchrotron, they would have presented similar curves, with or without trapping effects.
- ii)* There is no indication of $>$ one-second trapping when comparing the HXR curves at several energy bands and 15.4 GHz as it is illustrated in Figure 2.
- iii)* The similarities of the high-energy HXR and 15.4 GHz curves, *i.e.* presence of a number of peaks and lack of time delays, indicate that the electrons producing the microwave emission are not affected by magnetic trapping. It also suggests that the 15.4 GHz emission is mostly optically thin, and therefore, it is, at least, very close to the peak of the gyrosynchrotron spectrum. As noted before, the 212 GHz curve is smooth, and it does not follow the 15.4 GHz.
- iv)* A 25 second trapping is a rather extreme condition. A long trapping time has a strong impact in other source parameters, as the magnetic-field intensity. It has been shown by Giménez de Castro *et al.* (2009) that the greater the trapping time, for a given HXR flux, the smaller the magnetic field. A 25 s trapping would imply a magnetic field of a few Gauss, which would be too low to produce any significant emission at 212 GHz.
- v)* If the emission had been produced in an homogeneous source, the spectral index α between 15.4 and 212 GHz (Figure 1) would give us information on the electron distribution. However, during the event is always $\alpha < 0.5$, which would suggest a very hard, and unlikely, electron distribution with $\delta < 1.9$ (Dulk, 1985). Therefore, such a hard electron distribution is inconsistent with the value $\delta = 4.6$ derived from the HXR observed spectra. Moreover, a circumstantial indication supporting our conclusion is the absence of observational evidence for > 1 MeV electrons in the HXR data: the highest HXR energy detected significantly is ≈ 200 keV. It is well known that relativistic electrons are the main source of the 212 GHz synchrotron (*e.g.*, Ramaty *et al.*, 1994; Trotter *et al.*, 2015).

3.1. The Impulsive Phase

Taking into account all of the arguments presented above, we conclude that it is very unlikely that 212 GHz emission is due to gyrosynchrotron. This leaves thermal bremsstrahlung as the most likely mechanism to produce the observed 212 GHz radiation. The emission at these frequencies, during the gradual phase of flares, has been interpreted as due to thermal bremsstrahlung (Trotter *et al.*, 2002, 2011; Lüthi, Magun, and Miller, 2004; Lüthi, Lüdi, and Magun, 2004; Tsap *et al.*, 2016). Our observations and analysis put thermal bremsstrahlung as the dominating mechanism during the impulsive phase of SOL2011-02-14 as well.

It has been shown that ionized plasmas at $T < 1$ MK in the chromosphere are efficient mm-wave sources (Kašparová *et al.*, 2009; Heinzel and Avrett, 2012;

Simões *et al.*, 2017). In particular, Simões *et al.* (2017) have shown that once the energy deposition in the chromosphere stops, the free electrons quickly recombine with ions, thus reducing the main source of free–free emission after the impulsive phase. This decrease of the chromospheric emission could allow the optically thin free–free emission from the coronal plasma to dominate late in the gradual phase. and produce the microwave spectrum observed at the time intervals e and f in Figure 3.

Moreover, Trotter *et al.* (2015) interpreted that most of the 30 THz radiation observed during the flare SOL2012-03-13 is thermal bremsstrahlung of an optically thin source located above the temperature minimum in a $T \approx 8000$ K plasma heated by the energy deposited by precipitated particles (electrons, protons and α). Simões *et al.* (2017) have reached similar conclusions, using their results from numerical modeling to interpret the mid-infrared flare reported by Penn *et al.* (2016). Extending their calculations into the sub-THz range, they show that, during the impulsive phase, the sub-THz emission would be associated with the upper chromosphere with temperature around $T \approx 10^{4.6}$ K. Therefore, sub-THz as the thermal counterpart of the Neupert effect is certainly possible.

We present simple calculations to show that the observed flux density at 212 GHz can be easily explained by optically thick free–free emission originating in the upper chromosphere. The observed flare excess ΔS_f is simply the difference between the total flux during the flare S_f and pre-flare S_b , as observed by the SST 212 GHz beam:

$$\Delta S_f = S_f - S_b . \quad (5)$$

Using the Rayleigh–Jeans law, this becomes:

$$\Delta S_f = \frac{2k_b\nu^2}{c^2} \left(\frac{T_f A}{D^2} - T_\odot \Omega_b \right) \quad (6)$$

where c is the speed of light, T_\odot is the brightness temperature of the quiet Sun at $\nu = 212$ GHz, $\Omega_f = A/D^2$ is the solid angle of the flare, for an area A and $\Omega_b = 1.06 \cdot 10^{-6}$ str, is the solid angle of the 4' beam angular diameter, and finally D is the Sun–Earth distance, one astronomical unit (AU). With numerical values, $\Delta S_f = 220$ sfu, $T_s = 5,500$ K (Figure 3 of Selhorst, Silva, and Costa, 2005), and rearranging, Equation 6 becomes:

$$A_{20} = \frac{1.66}{T_4}, \quad (7)$$

where A_{20} is the flare area in 10^{20} cm² and T_4 is the brightness temperature at 212 GHz in 10^4 K.

Following the procedure introduced by Simões *et al.* (2017), we calculated the brightness temperature T_b at 212 GHz for two models of the F-CHROMA flare model database (www.fchroma.org/?page_id=24). The database contains more than 90 flare models and it was generated using the code RADYN (Carlsson and Stein, 1995; Allred, Kowalski, and Carlsson, 2015), starting from a quiet Sun atmospheric model based on VAL-C (Vernazza, Avrett, and Loeser, 1981).

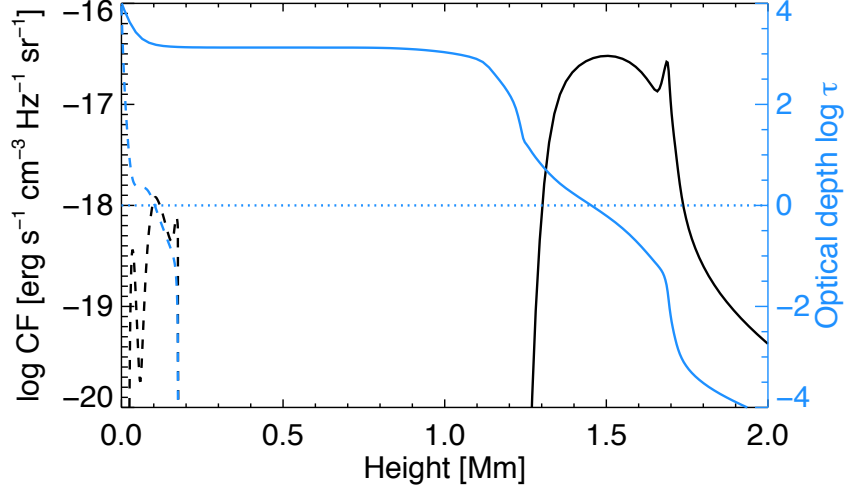


Figure 6. Contribution function [CF] (*black*) and optical depth τ (*blue*) at 212 GHz calculated from the F-CHROMA flare model 21, at the time of maximum energy input ($t = 10$ seconds, *continuous lines*) and pre-flare (*dashed lines*) for reference. The *dotted* horizontal line shows $\tau = 1$.

RADYN solves the coupled, non-linear, equations of hydrodynamics, atomic level populations, radiative transfer in a 1D atmosphere subject to energy input by a beam of accelerated electrons. The electron transport and energy deposition is treated by solving the Fokker–Planck equation for an initial electron power-law distribution with spectral index δ , low-energy cutoff E_c , with an energy flux F . We only present a brief description of the RADYN code here and note that Allred, Kowalski, and Carlsson (2015) should be consulted for more details.

We selected the models with electron-beam parameters closer to the ones estimated from the HXR spectral analysis, namely, Model 21 ($\delta = 5$, $E_c = 15$ keV, $F = 10^{10}$ erg s $^{-1}$ cm $^{-2}$), and Model 27 ($\delta = 5$, $E_c = 15$ keV, $F = 3 \times 10^{10}$ erg s $^{-1}$ cm $^{-2}$). The maximum T_b values found are $\approx 6.7 \times 10^4$ K and $\approx 10 \times 10^4$ K, for Models 21 and 27, respectively. Using these values for T_4 in Equation 7 gives an estimate of the necessary emitting areas to produced the observed flare emission of 220 sfu: $A = 2.5 \times 10^{19}$ and $A = 1.6 \times 10^{19}$ cm 2 , for Models 21 and 27, respectively.

The resulting contribution function [CF] and optical depth [τ] for 212 GHz are shown in Figure 6. [CF] indicates the formation height of the radiation (*e.g.*, Carlsson, 1998; Simões *et al.*, 2017), which originates near the base of the photosphere in the quiet Sun but shifts to the upper chromosphere during a flare. The emission is optically thick in both cases as indicated by the large optical depth $\tau > 1$.

The area of the flaring chromosphere can be estimated from AIA images. The best *Atmospheric Imaging Assembly* (AIA) band for this purpose is 1700 Å, since, unfortunately, most AIA bands saturate heavily during this event, es-

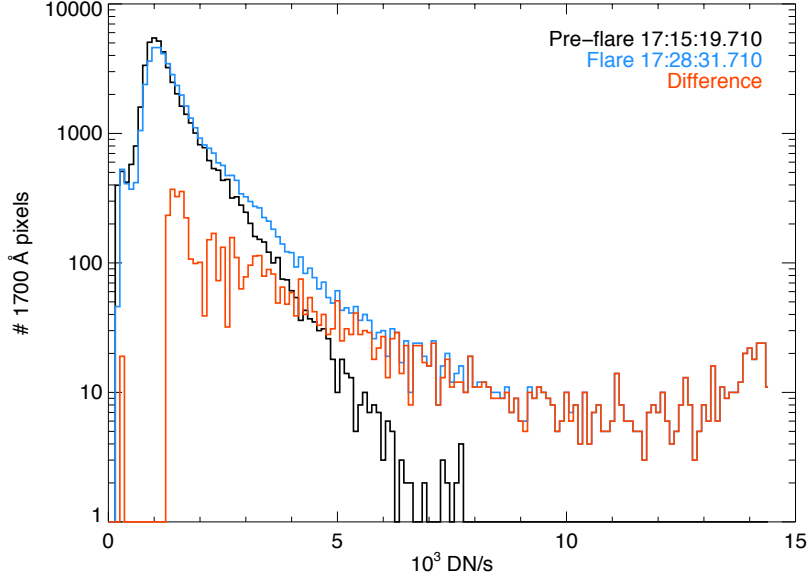


Figure 7. Histograms of pixel values [DN s^{-1}] of AIA 1700 Å images at pre-flare (*black*) and flare times (*blue*). We used their difference (*orange*) to estimate the number of flaring pixels and hence the flaring area.

pecially during the impulsive phase. According to Simões *et al.* (2019), the flare-excess emission captured by the AIA 1700 Å band originates in the chromosphere. To estimate the flaring area, we constructed histograms of AIA 1700 Å images and subtracted the average histogram of pre-flare images from the flare histograms. This resulted in the total number of pixels with values enhanced by the flare. The flaring area is then simply obtained by adding all the histogram bins and multiplying the result by the area relative to the AIA pixel ($0.6 \times 0.6 \text{ arcsec}^2$ corresponding to $\approx 1.9 \times 10^{15} \text{ cm}^2$). Ignoring the saturated images, we found an average area of $A \approx 2.6 \times 10^{19} \text{ cm}^2$, which is sufficient to produce the maximum observed flux density ($\approx 220 \text{ sfu}$), with the assumed T_4 values above; and also much bigger than the lower limit value A_{MB} obtained from the multi-beam technique.

These calculations are not an attempt to model this specific event. Our goal is show that typical flare characteristics are sufficient to generate an observable flare signature at sub-mm from optically thick free-free from the upper chromosphere.

3.2. The Gradual Phase

After the end of the HXR emission (around 17:26), the radio spectrum from microwaves to the submillimeter is consistent with thermal bremsstrahlung. Even if

we lack intermediate frequencies between 15.4 and 212 GHz to better characterize the spectrum, it is likely that for $\nu \geq 15$ GHz the emission is optically thin with a flux $F_{\text{gradual}} \approx 40 - 50$ SFU. From GOES data we obtain $EM_{\text{goes}} \sim 10^{49} \text{ cm}^{-3}$ and $T_{\text{goes}} \approx 16$ MK. If the radio source were coronal, it would produce a flux density at 212 GHz which is a tenth of the observed one. This problem was observed already in other works (*e.g.*, Lüthi, Magun, and Miller, 2004; Cristiani *et al.*, 2007). Trottet *et al.* (2011) addressed the same question for SOL2003-10-27T12:30 and solved the problem using a multi-thermal coronal source, where the lower layers are cooler. In this way the relatively high submillimeter density flux was explained. We note that SOL2003-10-27T12:30, an M6.7 GOES class event, has a gradual phase with a similar density flux at submillimeter frequencies as SOL2011-02-14, and that the GOES emission measure ($\approx 10^{49} \text{ cm}^{-3}$) and temperature (≈ 12 MK) are also quite similar. Therefore, conclusions from Trottet *et al.* (2011) can also be applied to this work.

3.3. Neupert Effect

We binned the *Fermi* NaI 128 energy channels in three HXR bands: 25–50 keV, 50–100 keV, and 100–300 keV. These bands were chosen in order to avoid the contribution from the thermal emission below 20 keV and the noise above 300 keV. We numerically integrated the HXR counts between $t_0 = 17:23$ UT and 17:32 UT. The resulting curves were compared with the 212 GHz flux-density temporal evolution (Figure 8, top left) and with the SXR GOES 1.5–12 keV and *Fermi* 12–25 KeV (Figure 8, bottom left). We note a coincidence between the maximum of the fluence 50–100 keV and the peak at 212 GHz. For the 25–50 keV band the fluence only reaches its maximum at the end of the time interval. Nonetheless it is worth to note that it follows the initial 212 GHz emission curve between 17:24 UT and 17:25 UT remarkably well. The association with SXR, however, is not so good. We observe that the SXR emission starts about 30 s before the HXR fluence. GOES 1.5–12 keV peak occurs simultaneously with the HXR fluence, meanwhile the *Fermi* 12–25 keV first peak is 30 seconds behind, only the second less intense peak is coincident with the fluence maximum.

We computed the time derivative (Equation 2) of the 212 GHz flux density using a three-point quadratic Lagrangian interpolation for unevenly spaced data and plotted its positive values along with the 50–100 keV count rate (Figure 8, top right panel). We have smoothed the 212 GHz data, using a 12 seconds running mean, to reduce the noise from the derivative procedure. Applying the same procedure to the SXR reveals a different behavior (Figure 8 bottom-right).

4. Conclusions

We present in this work a peculiar event observed at 212 GHz whose emission can be attributed to thermal bremsstrahlung during the impulsive and gradual phases. During the impulsive phase the 212 GHz emission comes from a thermal source at chromospheric heights. Moreover, its temporal derivative mimics the HXR flux (Figure 8, top-right), conforming with the thermal counterpart of

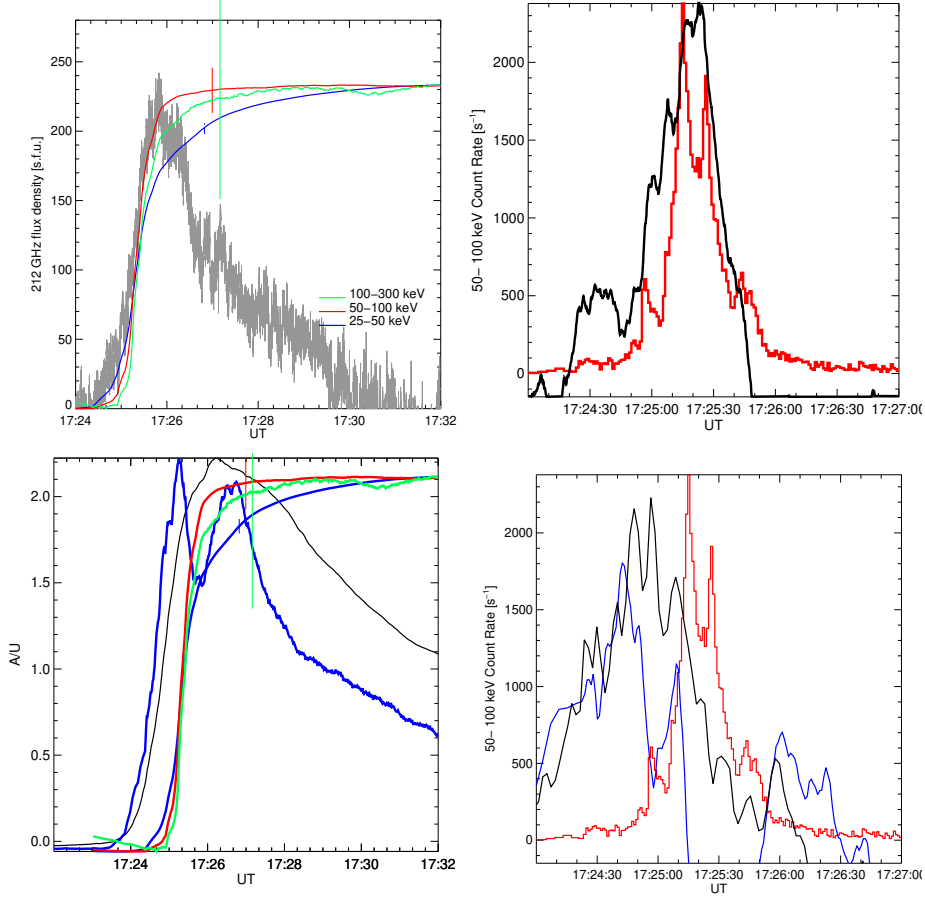


Figure 8. *Top-left:* The flux density at 212 GHz (gray) plotted along with the time integrated HXR count rate at three different energy bands: 25–50 keV (blue); 50–100 keV (red), and 100–300 keV (green). Vertical bars, with the same colors as the curves, represent their instantaneous uncertainty. *Top-right:* 50–100 keV count rate (red) plotted along with the 12 seconds smoothed 212 GHz flux-density tempoarl derivative (black) positive values. *Bottom-left:* the 1.5–12 keV GOES flux (black), plotted along with the 12–25 keV *Fermi* count-rate (blue), and the time-integrated HXR count-rate at the same three energy bands of the top panel. *Bottom-right:* 50–100 keV count rate (red) plotted along with the SXR temporal derivatives; blue is for GOES 1.5–12 keV, and black is for *Fermi* 9–12 keV count rate.

the Neupert effect. During the extended phase, the sub-THz emission might be characterized as optically thin thermal bremsstrahlung, from a coronal multi-thermal source as described by Trottet *et al.* (2011).

Differently from the sub-THz, in the SXR domain, we observe that during the event the emission starts well in advance of the HXR energy accumulation (Figure 8 bottom-left). Moreover, its temporal derivatives are significantly different from the HXR temporal evolution. This is not completely unexpected, since statistics show that 50 % of all events observed at SXR do not follow the Neupert effect hypothesis (Veronig *et al.*, 2002a). In our case, SXR starts before the HXR

fluence, which can be interpreted as a pre-heating of the plasma (Veronig *et al.*, 2005). That the temporal evolution of the sub-THz bremsstrahlung and SXR are not always coincident during a flare is already known (*e.g.* Trotter *et al.*, 2002; Tsap *et al.*, 2016), which explains why the Neupert effect is observed at 212 GHz and not at SXR.

We note that this is the first time that the iterative multi-beam technique has been used to deduce position, flux, and effective area with the SST. Cristiani *et al.* (2007), used the SST iterative method for point like sources, and the derived positions were compatible with the magnetic structures that originated the flare. In the present case, we found that in order to minimize the difference between expected and observed fluxes, the matrices $Q(t_i, x, y, \sigma_s)$, we need an extended source with $\varphi \geq 25''$. At the same time, and reinforcing the result, this solution is the closest to the main UV emitter (Figures 4 and 5). As we pointed out above, we don't find a unique solution here because we do not have four independent observations; we got a lower limit bound instead. The fact that this solution stabilizes above a threshold $\varphi \geq 25''$ is an indication of an extended source (Giménez de Castro *et al.*, 1999).

As a final remark, we stress the importance of the submillimeter and THz observing range for energy transport diagnostics in the solar atmosphere. Observations with the new instrumentation, at submillimeter frequencies (*e.g.* ALMA: Wedemeyer *et al.*, 2016), THz/infrared (Kaufmann *et al.*, 2013, 2016; Penn *et al.*, 2016), and/or near-infrared (Kleint *et al.*, 2016) should help the theoretical works to produce more refined flare models helping to increase our knowledge about the flaring solar atmosphere.

Acknowledgments The authors are grateful to Hugh Hudson for his enlightening comments about the Neupert effect and its history. J.F. Valle Silva acknowledges FAPESP for the support during his PhD Thesis (grant 2012/1619-9) and CAPES for the Postdoctoral PNPd contract. G. Giménez de Castro and J.-P. Raulin acknowledge CNPq (contracts 305203/2016-9 and 312066/2016-3). The research leading to these results has received funding from the European Community's Seventh Framework Program (FP7/2007-2013) under grant agreement no. 606862 (F-CHROMA), CAPES grant 88881.310386/2018-01, FAPESP grant 2013/24155-3 and the US Air Force Office for Scientific Research (AFOSR) grant FA9550-16-1-0072. AIA data is courtesy of NASA/SDO and the AIA, EVE, and HMI science teams. This work is based on data acquired at Complejo Astronómico El Leoncito, operated under agreement between the Consejo Nacional de Investigaciones Científicas y Técnicas de la República Argentina and the National Universities of La Plata, Córdoba and San Juan.

Disclosure of Potential Conflicts of Interest

The authors declare that they have no conflicts of interest.

References

- Allred, J.C., Kowalski, A.F., Carlsson, M.: 2015, A Unified Computational Model for Solar and Stellar Flares. *Astrophys. J.* **809**, 104. DOI. ADS.
- Antonucci, E., Gabriel, A.H., Dennis, B.R.: 1984, The energetics of chromospheric evaporation in solar flares. *Astrophys. J.* **287**, 917. DOI. ADS.
- Bastian, T.S., Benz, A.O., Gary, D.E.: 1998, Radio Emission from Solar Flares. *Annual Review of Astron. & Astrophys.* **36**, 131. ADS.
- Carlsson, M.: 1998, Radiative Transfer and Radiation Hydrodynamics. In: Vial, J.C., Bocchialini, K., Boumier, P. (eds.) *Space Solar Physics : Theoretical and Observational Issues in the Context of the SOHO Mission ; Proceedings of a summer school, held in Orsay, France, 1-13 September 1997*, **507**, 163. DOI. ADS.
- Carlsson, M., Stein, R.F.: 1995, Does a Nonmagnetic Solar Chromosphere Exist? *Astrophys. J. Lett.* **440**, L29. DOI. ADS.
- Costa, J.E.R., Silva, A.V.R., Lüdi, A., Magun, A.: 2002, Beam profile determination by tomography of solar scans. *Astron. Astrophys.* **387**, 1153. ADS.
- Cristiani, G., Martinez, G., Mandrini, C.H., Giménez de Castro, C.G., da Silva, C.W., Rovira, M.G., Kaufmann, P.: 2007, Spatial Characterization of a Flare Using Radio Observations and Magnetic Field Topology. *Solar Phys.*, 29. DOI. ADS.
- Dulk, G.A.: 1985, Radio emission from the sun and stars. *Annual Review of Astron. & Astrophys.* **23**, 169. ADS.
- Fleishman, G.D., Kontar, E.P.: 2010, Sub-THz Radiation Mechanisms in Solar Flares. *Astrophys. J. Lett.* **709**, L127. DOI. ADS.
- Frost, K.J.: 1964, Comments on High Energy X-Ray Bursts Observed by OSO I. *NASA SP* **50**, 139. ADS.
- Giménez de Castro, C.G., Raulin, J.-P., Makhmutov, V.S., Kaufmann, P., Costa, J.E.R.: 1999, Instantaneous positions of microwave solar bursts: Properties and validity of the multiple beam observations. *Astron. Astrophys. Suppl.* **140**, 373. ADS.
- Giménez de Castro, C.G., Trottet, G., Silva-Valio, A., Krucker, S., Costa, J.E.R., Kaufmann, P., Correia, E., Levato, H.: 2009, Submillimeter and X-ray observations of an X class flare. *Astron. Astrophys.* **507**, 433. DOI. ADS.
- Guidice, D.A., Cliver, E.W., Barron, W.R., Kahler, S.: 1981, The Air Force RSTN System. In: *Bull. Am. Astron. Soc.* **13**, 553. ADS.
- Heinzel, P., Avrett, E.H.: 2012, Optical-to-Radio Continua in Solar Flares. *Solar Phys.* **277**, 31. DOI. ADS.
- Herrmann, R., Magun, A., Costa, J.E.R., Correia, E., Kaufmann, P.: 1992, A multibeam antenna for solar mm-wave burst observations with high spatial and temporal resolution. *Solar Phys.* **142**, 157. ADS.
- Hudson, H.S.: 1991, Differential Emission-Measure Variations and the "Neupert Effect". In: *Bull. Am. Astron. Soc., Bulletin of the American Astron. Soc.* **23**, 1064. ADS.
- Hudson, H.S., Ohki, K.: 1972, Soft X-Ray and Microwave Observations of Hot Regions in Solar Flares. *Solar Phys.* **23**, 155. DOI. ADS.
- Kaufmann, P., Raulin, J.-P.: 2006, Can microbunch instability on solar flare accelerated electron beams account for bright broadband coherent synchrotron microwaves? *Physics of Plasmas* **13**, 701. DOI. ADS.
- Kaufmann, P., Levato, H., Cassiano, M.M., Correia, E., Costa, J.E.R., Giménez de Castro, C.G., Godoy, R., Kingsley, R.K., Kingsley, J.S., Kudaka, A.S., Marcon, R., Martin, R., Marun, A., Melo, A.M., Pereyra, P., Raulin, J.-P., Rose, T., Silva Valio, A., Walber, A., Wallace, P., Yakubovich, A., Zakia, M.B.: 2008, New telescopes for ground-based solar observations at submillimeter and mid-infrared. In: *Soc. Photo-Opt. Instrum. Eng. (SPIE) CS* **7012**. DOI. ADS.
- Kaufmann, P., White, S.M., Freeland, S.L., Marcon, R., Fernandes, L.O.T., Kudaka, A.S., de Souza, R.V., Aballay, J.L., Fernandez, G., Godoy, R., Marun, A., Valio, A., Raulin, J.-P., Giménez de Castro, C.G.: 2013, A Bright Impulsive Solar Burst Detected at 30 THz. *Astrophys. J.* **768**, 134. DOI. ADS.
- Kaufmann, P., Abrantes, A., Bortolucci, E., Caspi, A., Fernandes, L.O.T., Kropotov, G., Kudaka, A., Laurent, G.T., Machado, N., Marcon, R., Marun, A., Nicolaev, V., Hidalgo Ramirez, R.F., Raulin, J.-P., Saint-Hilaire, P., Shih, A., Silva, C., Timofeevsky, A.: 2016, Solar Observations at THz Frequencies on Board of a Trans-Antarctic Stratospheric Balloon Flight. In: *AAS/Solar Phys. Div. Meet.* **47**, 6.11. ADS.

- Kašparová, J., Heinzel, P., Karlický, M., Moravec, Z., Varady, M.: 2009, Far-IR and Radio Thermal Continua in Solar Flares. *Central European Astrophysical Bulletin* **33**, 309. ADS.
- Kleint, L., Heinzel, P., Judge, P., Krucker, S.: 2016, Continuum Enhancements in the Ultraviolet, the Visible and the Infrared during the X1 Flare on 2014 March 29. *Astrophys. J.* **816**, 88. DOI. ADS.
- Krucker, S., Giménez de Castro, C.G., Hudson, H.S., Trottet, G., Bastian, T.S., Hales, A.S., Kašparová, J., Klein, K.-L., Kretschmar, M., Lüthi, T., Mackinnon, A., Pohjolainen, S., White, S.M.: 2013, Solar flares at submillimeter wavelengths. *Astron. Astrophys. Rev.* **21**, 58. DOI. ADS.
- Lüthi, T., Lüdi, A., Magun, A.: 2004, Determination of the location and effective angular size of solar flares with a 210 GHz multibeam radiometer. *Astron. Astrophys.* **420**, 361. ADS.
- Lüthi, T., Magun, A., Miller, M.: 2004, First observation of a solar X-class flare in the submillimeter range with KOSMA. *Astron. Astrophys.* **415**, 1123. ADS.
- McAteer, R.T.J., Bloomfield, D.S.: 2013, The Bursty Nature of Solar Flare X-Ray Emission. II. The Neupert Effect. *Astrophys. J.* **776**, 66. DOI. ADS.
- Meegan, C., Lichti, G., Bhat, P.N., Bissaldi, E., Briggs, M.S., Connaughton, V., Diehl, R., Fishman, G., Greiner, J., Hoover, A.S., van der Horst, A.J., von Kienlin, A., Kippen, R.M., Kouveliotou, C., McBreen, S., Paciesas, W.S., Preece, R., Steinle, H., Wallace, M.S., Wilson, R.B., Wilson-Hodge, C.: 2009, The Fermi Gamma-ray Burst Monitor. *Astrophys. J.* **702**, 791. DOI. ADS.
- Neupert, W.M.: 1968, Comparison of Solar X-Ray Line Emission with Microwave Emission during Flares. *Astrophys. J. Lett.* **153**, L59. DOI. ADS.
- Penn, M., Krucker, S., Hudson, H., Jhabvala, M., Jennings, D., Lunsford, A., Kaufmann, P.: 2016, Spectral and Imaging Observations of a White-light Solar Flare in the Mid-infrared. *Astrophys. J. Lett.* **819**, L30. DOI. ADS.
- Pick, M., Vilmer, N.: 2008, Sixty-five years of solar radioastronomy: flares, coronal mass ejections and Sun Earth connection. *Astron. Astrophys. Rev.* **16**, 6. DOI. ADS.
- Ramaty, R., Schwartz, R.A., Enome, S., Nakajima, H.: 1994, Gamma-ray and millimeter-wave emissions from the 1991 June X-class solar flares. *Astrophys. J.* **436**, 941. ADS.
- Selhorst, C.L., Silva, A.V.R., Costa, J.E.R.: 2005, Solar atmospheric model with spicules applied to radio observation. *Astron. Astrophys.* **433**, 365. DOI. ADS.
- Silva, A.V.R., Laganá, T.F., Gimenez Castro, C.G., Kaufmann, P., Costa, J.E.R., Levato, H., Rovira, M.: 2005, Diffuse Component Spectra of Solar Active Regions at Submillimeter Wavelengths. *Solar Phys.* **227**, 265. DOI. ADS.
- Simões, P.J.A., Kerr, G.S., Fletcher, L., Hudson, H.S., Giménez de Castro, C.G., Penn, M.: 2017, Formation of the thermal infrared continuum in solar flares. *Astron. Astrophys.* **605**, A125. DOI. ADS.
- Simões, P.J.A., Reid, H.A.S., Milligan, R.O., Fletcher, L.: 2019, The Spectral Content of SDO/AIA 1600 and 1700 Å Filters from Flare and Plage Observations. *Astrophys. J.* **870**(2), 114. DOI. ADS.
- Trottet, G., Rolli, E., Magun, A., Barat, C., Kuznetsov, A., Sunyaev, R., Terekhov, O.: 2000, The fast and slow H α chromospheric responses to non-thermal particles produced during the 1991 March 13 hard X-ray/gamma-ray flare at \sim 08 UTC. *Astron. Astrophys.* **356**, 1067. ADS.
- Trottet, G., Raulin, J.-P., Kaufmann, P., Siarkowski, M., Klein, K.-L., Gary, D.E.: 2002, First detection of the impulsive and extended phases of a solar radio burst above 200 GHz. *Astron. Astrophys.* **381**, 694. ADS.
- Trottet, G., Raulin, J.-P., Giménez de Castro, C.G., Lüthi, T., Caspi, A., Mandrini, C., Luoni, M.L., Kaufmann, P.: 2011, Origin of the submillimeter radio emission during the time-extended phase of a solar flare. *Solar Phys.* **273**(2), 340. DOI.
- Trottet, G., Raulin, J.-P., Mackinnon, A., Giménez de Castro, G., Simões, P.J.A., Cabezas, D., de La Luz, V., Luoni, M., Kaufmann, P.: 2015, Origin of the 30 THz Emission Detected During the Solar Flare on 2012 March 13 at 17:20 UT. *Solar Phys.* **290**, 2809. DOI. ADS.
- Tsap, Y.T., Smirnova, V.V., Morgachev, A.S., Motorina, G.G., Kontar, E.P., Nagnibeda, V.G., Strekalova, P.V.: 2016, On the origin of 140 GHz emission from the 4 July 2012 solar flare. *Adv. Space Res.* **57**, 1449. DOI. ADS.
- Vernazza, J.E., Avrett, E.H., Loeser, R.: 1981, Structure of the solar chromosphere. III - Models of the EUV brightness components of the quiet-sun. *Astrophys. J. Suppl. Ser.* **45**, 635. DOI. ADS.

- Veronig, A.M., Brown, J.C., Dennis, B.R., Schwartz, R.A., Sui, L., Tolbert, A.K.: 2005, Physics of the Neupert Effect: Estimates of the Effects of Source Energy, Mass Transport, and Geometry Using RHESSI and GOES Data. *Astrophys. J.* **621**, 482. DOI. ADS.
- Veronig, A., Vršnak, B., Dennis, B.R., Temmer, M., Hanslmeier, A., Magdalenic, J.: 2002a, Investigation of the Neupert effect in solar flares. I. Statistical properties and the evaporation model. *Astron. Astrophys.* **392**, 699. DOI. ADS.
- Veronig, A., Vršnak, B., Temmer, M., Hanslmeier, A.: 2002b, Relative timing of solar flares observed at different wavelengths. *Solar Phys.* **208**, 297. DOI. ADS.
- Wedemeyer, S., Bastian, T., Brajša, R., Hudson, H., Fleishman, G., Loukitcheva, M., Fleck, B., Kontar, E.P., De Pontieu, B., Yagoubov, P., Tiwari, S.K., Soler, R., Black, J.H., Antolin, P., Scullion, E., Gunár, S., Labrosse, N., Ludwig, H.-G., Benz, A.O., White, S.M., Hauschildt, P., Doyle, J.G., Nakariakov, V.M., Ayres, T., Heinzel, P., Karlicky, M., Van Doorselaere, T., Gary, D., Alissandrakis, C.E., Nindos, A., Solanki, S.K., Rouppe van der Voort, L., Shimojo, M., Kato, Y., Zaqarashvili, T., Perez, E., Selhorst, C.L., Barta, M.: 2016, Solar Science with the Atacama Large Millimeter/Submillimeter Array-A New View of Our Sun. *Space Sci. Rev.* **200**, 1. DOI. ADS.
- White, W.A.: 1964, Solar X Rays: A Comparison With Microwave Radiation. *NASA SP* **50**, 131. ADS.